Metabolic Insights into Iron Deposition in Relapsing-Remitting Multiple Sclerosis via 7T Magnetic Resonance Spectroscopic Imaging

Alexandra Lipka, MSc[1]; Wolfgang Bogner, PhD[1]; Assunta Dal-Bianco, MD[2]; Gilbert J. Hangel, PhD[1,3]; Paulus S. Rommer, MD[2]; Bernhard Strasser, PhD[1]; Stanislav Motyka, PhD[1]; Lukas Hingerl, PhD[1]; Thomas Berger, MD, MSc[2]; Fritz Leutmezer, MD[2]; Stephan Gruber, PhD[1]; Siegfried Trattnig, MD[1,4]; and Eva Niess, PhD[1]

[1] High Field MR Centre, Department of Biomedical Imaging and Image-guided Therapy, Medical University of Vienna, Vienna, Austria

[2] Department of Neurology, Medical University of Vienna, Vienna, Austria

[3] Department of Neurosurgery, Medical University of Vienna, Vienna, Austria

[4] Karl Landsteiner Institute for Clinical Molecular MRI in Musculoskeletal System, Vienna, Austria

Institutional address: High Field MR Centre, Department of Biomedical Imaging and Image-guided Therapy, Medical University of Vienna, Lazarettgasse 14, A-1090 Vienna, Austria

*** Corresponding author:** Wolfgang Bogner; High Field MR Centre, Department of Biomedical Imaging and Image-guided Therapy, Medical University of Vienna, Lazarettgasse 14, A-1090 Vienna, Austria; wolfgang.bogner@meduniwien.ac.at, +43(0)140400-64710

ABSTRACT

Objective

To investigate the metabolic pattern of different types of iron accumulation in multiple sclerosis(MS) lesions, and compare metabolic alterations within and at the periphery of lesions and newly emerging lesions *in vivo* according to iron deposition.

Methods

7T MR spectroscopic imaging and susceptibility-weighted-imaging was performed in 31 RRMS patients(16female/15male;mean age,36.9±10.3years). Mean metabolic ratio were calculated for regions of interest(ROI) of normal appearing white matter(NAWM), “non-iron”, and three distinct types of iron-laden lesions, and for lesion layers of “non-iron” and “rim” lesions. Furthermore, newly emerging “non-iron” and “iron” lesions were compared longitudinally.

Results

52% of iron-containing lesions showed no distinct paramagnetic rim. Of these, “area” lesions exhibited a 65% higher mIns/tNAA(p=0.035) than “rim” lesions. Comparing lesion layers of both “non-iron” and “rim” lesions, a steeper metabolic gradient of mIns/tNAA(“non-iron”+15%,“iron”+40%) and tNAA/tCr(“non-iron”-15%,“iron”-35%) was found in “iron” lesions, with the lesion core showing +22% higher mIns/tNAA(p=0.005) and -23% lower tNAA/tCr(p=0.048) in “iron” compared to “non-iron” lesions. In newly emerging lesions, 46% showed iron accumulation, with the drop in tNAA/tCr after lesion formation remaining significantly lower compared to pre-lesional tissue over time in “iron” lesions(year0:p=0.013,year1:p=0.041) as opposed to “non-iron” lesions(year0:p=0.022,year1:p=0.231).

Conclusion

7T MRSI allows in vivo characterization of different iron accumulation types showing metabolic differences. Furthermore, the larger extent of neuronal damage in lesions with a distinct iron rim was reconfirmed, but with metabolic differences in lesion development between (non)-iron-containing lesions. This highlights the ability of MRSI to further investigate different types of iron accumulation and suggests possible implications for disease monitoring.

Clinical relevance statement:

The clinical importance of differentiating various types of iron accumulation in MS lesions was shown, as contrasting metabolic profiles are likely associated with different levels of tissue damage.

Key points:

- Iron-containing lesions were suggested as a biomarker for tissue damage, a more aggressive disease course, and worse clinical outcome, but related metabolic alterations are poorly understood
- Our MRSI results confirm a higher extent of tissue damage within paramagnetic rim lesions. 46% of newly emerging lesions showed an iron accumulation, correlating with an altered metabolic behavior compared to non-iron lesions
- Only 48% of iron-containing lesions have a distinct rim-shaped iron accumulation, although most studies focus on these paramagnetic rim lesions. We showed highly different metabolic profiles in different iron accumulation types, highlighting the need for distinct classification of iron accumulation

Key words: Magnetic Resonance Spectroscopy, Multiple Sclerosis, brain, demyelination

Abbreviations:

EDSS = Expanded Disability Status Scale

mIns = myo-inositol

tNAA = total N-acetyl aspartate

FID-MRSI = free-induction decay magnetic resonance spectroscopic imaging

MS = multiple sclerosis

NAWM = normal-appearing white matter

SWI = Susceptibility Weighted Imaging

tCr = total creatine

tCho = total choline

Introduction

Conventional T1- and T2-weighted magnetic resonance imaging (cMRI) is an integral part of diagnosis and treatment monitoring in Multiple Sclerosis (MS)[1]–[3]. Yet, the biggest drawback of cMRI measures is the lack of strong correlation with disability status[4]. Currently established MRI techniques are not specific enough to assess the underlying pathological process, as they are sensitive only to macroscopic tissue damage. MR Spectroscopic Imaging (MRSI), however, can visualize pathology on a biochemical level by mapping the spatial distribution of various brain metabolites[5], [6]. The most commonly reported abnormalities found in MS are decreased N-acetylaspartate (NAA; reflecting reduced neuronal/axonal integrity and function) and increased myo-inositol (mIns; a marker for astroglial hypertrophy and hyperplasia), which correlates with clinical impairment, and elevated choline (Cho; a marker of myelin turnover)[7]–[9]. Susceptibility Weighted Imaging (SWI) can provide additional information about tissue microstructure and, specifically, iron deposition. Iron deposition has been described in a subset of chronically active lesions, which are usually defined as having a demyelinated core surrounded by a rim of reactive astrocytes and iron-laden microglia/macrophages[10] hypointense on SWI. These so-called iron-rim lesions have been linked to tissue damage, a more progressive disease course, and, thus, a worse clinical outcome[11]–[15].

A recent review article[10] has suggested iron-containing lesions as a new lesion biomarker for MS[16], as those lesions can be found in a high proportion of MS patients regardless of their clinical phenotype[12], [15], [17], [18]. Furthermore, the high specificity of this technique to differentiate MS from MS-mimicking diseases[19], [20] and the potential to predict the conversion from radiologically isolated syndrome[21] and clinically isolated syndrome[22] has been shown.

Iron-containing lesions have mostly been studied regardless of their iron deposition subtype[23], [24] and their characteristic slow expansion is currently controversially discussed[25]–[27]. 7T MRI can, due to its higher spatial resolution, differentiate between iron-containing lesions with a distinct paramagnetic rim and those with a diffuse iron accumulation that involves the whole lesion[11]. Furthermore, the higher spatial resolution at 7T enables the study of metabolic alterations during lesion development[28].

Metabolic alterations as measured by MRSI have–to the best of our knowledge–never been correlated with iron deposition. Therefore, we aim to: (1) characterize different types of iron-containing lesions and determine the differences in their metabolic alterations; (2) investigate differences in metabolic alterations inside and at the periphery of iron- and non-iron-containing lesions; and (3) identify metabolic differences in newly emerging iron- and non-iron-containing lesions.

Materials and Methods

Study Population

For this prospective study, written, informed consent and IRB approval (EK 154/2009) were obtained. Patient recruitment by the Department of Neurology took place between January 2016 and December 2017 and fulfilled the following criteria: clinically definite MS diagnosis according to revised McDonald criteria[1]; no change in the Expanded Disability Status Scale (EDSS) score[29] during the prior six months; stable/no treatment during the prior six months; no relapse or corticosteroid treatment within the prior three months; no other neuropsychiatric or neurological disease; and no 7T-MRI contraindications (Figure 1).

Imaging Protocol

All measurements were performed on the same 7T whole-body MR scanner (Magnetom, Siemens Healthcare, Erlangen, Germany) using a 1TX/32RX head coil (Nova Medical, Wilmington, MA). Each session included three-dimensional T_1-weighted imaging using two magnetization-prepared rapid gradient echoes (MP2RAGE) (TR=5000ms, TE=4.13ms, TI1/TI2=700ms/2700ms, scan time=8:02min) with 0.8×0.8×0.8mm^3 spatial resolution, three-dimensional T_2-weighted imaging using fluid-attenuated inversion recovery (FLAIR) (TR=8000ms, TE=270ms, TI=2180ms, scan time=7:14min) with 0.86x0.86x0.86 mm^3 spatial resolution, and three-dimensional susceptibility weighted imaging (SWI) (TR=38ms, TE=25ms, scan time=7:24min) with 0.3×0.3×1.2mm^3 spatial resolution to visualize MS lesions and potential iron deposition prior to positioning of the MRSI volume of interest. A single-slice, transversal, two-dimensional free induction decay MRSI[30] scan was obtained above the corpus callosum with an acquisition delay/repetition time of 1.3ms/200ms, an Ernst flip angle of 27°, four-fold parallel imaging acceleration via Controlled Aliasing in Parallel Imaging Results in Higher Acceleration(CAIPIRINHA)[31], a field of view of 220×220mm^2 , a matrix size of 100×100, a nominal voxel size of 2.2×2.2×8mm^3, an effective voxel volume of 77µl, and a scan time of 6:06min[30], [32]. Additional data acquisition details can be found in Suppl. Table 1.

Spectroscopic Data Processing

After extracting brain masks from T_1-weighted images using the FSL brain extraction tool[33], MRSI data were processed with an automated in-house-developed post-processing pipeline using Matlab (R2013a | Mathworks, Natick, MA), MINC (v2.0 | McConnell Brain Imaging Center, Montreal, Quebec, Canada) and Bash (v4.2.25 | Free Software Foundation, Boston, MA). The

pipeline included MUSICAL coil combination[34], 2D-CAIPIRINHA reconstruction[31], lipid signal removal via L2-regularization[35], and spatial Hamming filtering. Using a basis-set of 17 simulated metabolites[36] and a measured macromolecular background[37], individual spectra were fitted in the spectral range of 1.8-4.2 ppm with LCModel (version 6.3-1; http://s-provencher.com/lcmodel.shtml). Afterward, metabolic maps and their ratios, quantification precision [i.e., Cramer-Rao Lower Bounds (CRLBs)], spectral quality [i.e., FWHM (linewidth as full-width-half-maximum of the fitted NAA peak), SNR (signal-to-noise ratio of the fitted NAA peak)] were created (Suppl. Table 2). MRS data reporting followed standardized guidelines[38] (Suppl. Table 1).

Data Analysis

Segmentation and iron accumulation type categorization

After resampling (via tricubic interpolation) of metabolic maps to the resolution of T1-weighted images, lesion and representative (fixed volume of 37mm^3, minimum distance of 0.5cm to GM/CSF/lesions) normal-appearing white matter "NAWM" ROIs were segmented via the user-guided, semi-automatic segmentation software ITK–SNAP[39]. Based on SWI images, ROIs were categorized into four iron accumulation types by two authors individually (A.D.B with 10 years of experience, A.L. with three years of experience) if the iron deposition spanned three contiguous layers: (a) "rim" (distinct rim-shaped iron deposition); (b) "area" (iron accumulation covering the entire lesion); (c) "transition" (transition between "area" to "rim" shape); and (d) "non iron" if no iron accumulation was present (Figure 2). For the final analysis, only lesions exceeding 20mm^3 were included to mitigate the influence of partial volume errors.

Layer analysis

To investigate whether the metabolic profile within and in the proximity of MS lesions differed between “non-iron” and “rim” lesions, the segmented ROIs of these categories were both dilated and eroded three times. This resulted in seven lesion layer rings in total, spanning from the outermost layer (L+3) to the innermost layer (L-3), each ~1mm thick. Voxels that potentially intruded into the GM and CSF after dilation were handled in the following way: lesion-free GM and CSF masks (created using Freesurfer and mincmath) were subtracted from the respective ROIs; where needed, manual correction for GM, CSF and voxels of neighboring lesions was performed using FSLView (Figure 5A). Because at least four lesion layers were required to “fit” inside the lesion, only lesions of an original size of 100-400mm3 were included. For each lesion, metabolic ratios were normalized to NAWM (represented by the respective outermost lesion layer).

Longitudinal analysis of newly emerging lesions

As the patient cohort overlapped with a previous longitudinal study[24], morphological imaging data for additional time points were available. Thus, it was possible to identify newly emerging lesions and determine their age. These lesions—if spectroscopic data was available for the respective time point—were segmented and the metabolic patterns within each ROI were evaluated at all timepoints (i.e., prior and after appearance of the lesion on cMRI). The following time point ROIs were evaluated: “Year -1” (NAWM with the same position and size as the lesion occurring in Year 0); “Year 0” (newly identified lesion); and “Year 1” (follow-up measurement after one year). All these lesions were categorized according to their iron accumulation type (“non-iron” vs. “iron”).

Statistics

Statistical analysis was performed using IBM SPSS 24. For all ROIs, descriptive statistics for multiple metabolic ratios (mIns/tNAA, Ins/tCr, tNAA/tCr, tCho/tCr) were derived. Using one-way ANOVA and Tukey post-hoc analysis ($p<0.05$ considered as statistically significant), metabolite levels between iron accumulation types, lesion layers ("rim" vs "non-iron" lesions), and newly emerging lesions ("Year -1" vs "Year 0" vs "Year 1" & "all new" vs "iron" vs "non-iron") were compared. All values are listed as mean+-SD unless stated otherwise.

Results

Thirty-one patients with relapsing-remitting MS (16 female/15 male; mean age, 36.9 ± 10.3 years), were included in the final study. Patient demographics, including medications and EDSS scores (assessed in consensus by two experienced neurologists; A.DB, P.R), were collected (Table 1). In total, 487 ROIs were segmented: 412 "non-iron"; 31 "area;" eight "transition;" and 36 "rim.".Of the 487 lesion ROIs, 220 fulfilled the minimum size criterion and were included in the final analysis (174 "non-iron," 13 "area," seven "transition," and 26 "rim"). Forty-four "non-iron" and eight "rim" fulfilled the minimum size criterion for the layer analysis. For the newly emerging lesion analysis, 39 new lesions were identified in seven patients, with 27 having available spectroscopic data, resulting in 11 "non-iron" and 16 "iron" lesions analyzed (Table 2). The spectral quality was high and, even though NAA is reduced by pathology, the mean SNR of NAA ranged from 11-15, and the mean FWHM of NAA ranged from 19.6-21.4Hz, while the average CRLB values (mIns, tCho, tCr, tNAA) ranged from 15-26% (Suppl. Table 2).

Iron accumulation type comparison

Differences in mIns/tNAA were the most prominent metabolic distinction between different iron accumulation types (Table 3, Figure 3&4): “rim” lesions had, on average, 35% higher mIns/tNAA than “non-iron” (1.53±0.97 vs. 1.13±0.58, p=0.02) and 65% higher mIns/tNAA than “area” lesions (0.93±0.30, p=0.035). Furthermore, in both “non-iron” (1.13±0.58, p≤0.0001) and “rim” (1.53±0.97, p≤0.0001) lesions, mIns/tNAA was higher than in “NAWM” (0.53±0.17).

For mIns/tCr, no differences were found between “rim” (1.19±0.37) lesions and other lesion types (vs. “non-iron” p=0.615; vs. “area” p=1.00), but mIns/tCr was higher than that in “NAWM” (0.85±0.30, p=0.005). mIns/tCr in “NAWM” was also lower compared to “non-iron” (1.08±0.36, p=0.012) and “area” (1.19±0.49, p=0.040) lesions. “Area” was not different from “non-iron” (p=0.823) and “transition” (1.14±0.38) did not show any differences (vs. “NAWM” p=0.311; vs. “non-iron” p=0.991; vs. “area” p=0.999; vs. “rim” p=0.998).

In “NAWM,” the tNAA/tCr (1.67±0.37) was higher than in “non-iron” (1.08±0.39, p≤0.001), “rim” (1.00±0.47, p≤0.001), and “transition” (1.14±0.38, p=0.035) lesions. There were no differences in NAA/tCr between iron-deposition categories, although there was a trend toward higher NAA/tCr in “rim” vs. “area” lesions (1.19±0.49,p=0.051).

Compared to “NAWM” (0.46±0.08), there was lower tCho/tCr in “rim” (0.40±0.10, p=0.009) lesions; however this was not the case in “non-iron” (0.42±0.07, p=0.056) lesions.

Lesion periphery

All reported results (Table 4, Figure 5B) were achieved through normalization using the outermost layer, thus resulting in all L+3 layers having a value of 1.00±0.00 and no comparisons of L+3 between “iron” and “non-iron” being considered.

Differences between lesion layers within and between iron accumulation types were found for mIns/tNAA and tNAA/tCr between layers L-3 and L+3.

In the “non-iron” lesions subgroup, there was a 15.2% higher mIns/tNAA in the innermost layer (L-3) than in the outermost layer (L+3) (1.15±0.26 vs. 1.00±0.00, p≤0.01). In contrast, the group of “rim” lesions had a 40.22% higher mIns/tNAA in the L-3 compared to the L+3 layer (1.40±0.34 vs. 1.00±0.00, p≤0.001).

Between the groups (“rim” vs. “non-iron”), “rim” exhibited a 21.71% higher mIns/tNAA for L-3 compared to “non-iron” (mean±SD: 1.40±0.34 vs. 1.15±0.26, p=0.005).

For tNAA/tCr, an inverse behavior was observed. In the “non-iron” group, L-3 had a -14.94% lower tNAA/tCr than L+3 (0.85±0.29 vs. 1.00±0.00, p≤0.001). In the “rim” group, L-3 exhibited a -34.73% lower tNAA/tCr compared to L+3 (0.65±0.16 vs. 1.00±0.00, p≤0.001). Between the groups, tNAA/tCr of the L-3 layer was -23.27% lower in “rim” than in “non-iron” lesions (0.65±0.16 vs. 0.85±0.29, p=0.048)

For both mIns/tCr and tCho/tCr, no differences within or between the groups were significant.

Newly emerging lesions

Significant differences in newly emerging lesions were found for mIns/tNAA and tNAA/tCr (Table 5, Figure 6).

A 69.6% increase of mIns/tNAA was observed in newly identified lesions between “Year -1” and “Year 1” (0.74±0.31 vs. 1.26±0.76, p=0.049). There was no difference in mIns/tNAA between “Year -1” and “Year 0” (0.74±0.31 vs. 1.17±0.41, p=0.126) or between “Year 0” and “Year 1” (1.17±0.41 vs. 1.26±0.76, p=0.904).

No differences were found in mIns/tCr during lesion development.

The most significant changes during lesion development were found for tNAA/tCr: in the group of all new lesions, “Year 0” (0.90±0.20, p≤ 0.001) and “Year 1” (0.97±0.31, p=0.006) were lower by -31% and -26% ,respectively, compared to “Year -1” (1.30±0.34). In “iron” lesions, tNAA/tCr was lower by -31% and -24%, respectively, in “Year 0” (0.84±0.19, p=0.013) and “Year 1” (0.92±0.27, p=0.041) when compared to “Year -1” (1.21±0.29). In “non-iron” lesions, tNAA/tCr of “Year 0” was -34% lower than that of “Year -1”(1.42±0.38 vs. 0.95±0.20, p=0.022), while there were no significant differences between “Year -1” vs. “Year 1” (1.08±0.41, p=0.231).

For tCho/tCr, no significant results were found.

Discussion

This study evaluated the frequency of iron deposition types and the occurrence of iron accumulation in newly emerging lesions in 31 RRMS patients at 7T. It further evaluated metabolic alterations within these different iron deposition types, inside and in the proximity of (non)-iron-containing lesions and the longitudinal metabolic changes during the early development of lesions according to their iron status.

We found that less than half (48%) of iron-containing lesions showed a distinct paramagnetic rim of iron accumulation and that 46% of lesions already showed iron accumulation when newly emerging. Furthermore, MS lesions were clearly visualized on high-resolution metabolic maps, especially for tNAA/tCr and mIns/tNAA ratios. These prominent findings are attributed to the combined effect of decreased tNAA, associated with neuronal damage, axonal loss, and mitochondrial dysfunction, as well as increased mIns, which reflects astroglial activation.

In general, all MS lesions showed metabolic differences compared to NAWM. The metabolic changes between non-iron and iron-containing lesions were driven by both tNAA and mIns,

while most axonal damage was found in iron-containing lesions with a distinct rim[40]. Looking into the other iron accumulation subgroups, the “transition” type is both macroscopically and metabolically an intermediate between iron rim lesions and iron-containing lesions with a diffuse iron accumulation. These “area” lesions interestingly showed a 38% higher tNAA/tCr compared to iron rim lesions and a 27% higher tNAA/tCr compared to non-iron lesions, possibly representing an intrinsic attempt to enhance neural integrity, supporting the presumed role of iron as a co-regulator of remyelination[41]. Unfortunately, the number of “area” lesions that met the minimum volume criterion was low. Thus, only 42% could be evaluated in the final analysis, resulting in an underpowered, and thus, non-significant statistical comparison to rim lesions. The finding of increased tNAA/tCr in “area” lesions is in agreement with a previous preliminary study[42]. Nevertheless, these previous preliminary results, as well as the frequency of iron-containing lesions without a distinct rim and their different metabolic profiles, highlights the importance of characterizing iron-containing lesions into distinct groups[11], as different types of iron accumulation might have a different influence on disease course.

We also investigated metabolic profiles inside and at the periphery of lesions. A steeper metabolic gradient (i.e., higher mIns/tNAA and lower tNAA/Cr in the center) was found for rim lesions compared to non-iron lesions. We found that tNAA reduction is the predominant differentiator between non-iron and rim lesions. This reconfirms histological studies[15], [43] that reported more damage inside iron rim lesions and the role of tNAA as a biomarker for tissue damage[28], explaining the worse clinical outcome[12] in patients with distinct rim-shaped iron-accumulating lesions. Nevertheless, we did not find any difference between non-iron and rim lesions with regard to mIns[28], which would have confirmed the importance of iron rims in the ongoing debate on slowly expanding lesions [25]–[27].

We found reduced tNAA in newly emerging lesions regardless of iron accumulation, confirming results by Kirov et al.[44] in persistent lesions, although their study incorporated only three

lesions and did not differentiate between iron accumulation types. Looking into our one-year follow-up scans, tNAA showed a re-elevation in non-iron lesions, while it remained reduced in iron-containing lesions, similar to the results of Kirov et al.[44] for resolving lesions, although their study was performed using a much lower spatial and spectral resolution. Our results, therefore, reconfirm the higher damage in iron-containing lesions and their reduced remyelination, although for this analysis–due to the low number of newly emerging lesions–no difference between iron accumulation types was found. Furthermore, the longitudinal assessment of mIns in our study suggests that mIns might have a larger influence on earlier lesion development in iron-containing lesions compared to non-iron lesions, potentially reflecting a higher accumulation of reactive astroglia. Even though not many newly emerging lesions were found due to the patient population having a stable disease course, almost half the lesions did show iron accumulation from the beginning, which might be the determining factor in disease progression[15], [43], [45]–[48].

In addition to the already mentioned limited sample size of “area” and newly emerging lesions, our study has some further limitations. As our MRSI sequence was limited to a single 8-mm thick slice above the corpus callosum and bias due to partial volume effects had to be avoided, the number of included lesions was limited. To overcome the limitation of a single-slice acquisition, a 3D-MRSI version of this sequence, covering the majority of the brain, has recently been introduced and has provided promising results in brain tumors[6], [49]. In addition, we did not determine concentration estimates, as we could not avert changes in the T1 relaxation times due to MS pathology[50] and an additional water scan would have doubled our scan time for each slice.

In this study, we observed metabolic alterations that were associated with iron deposition in MS lesions. In particular, we found lower tNAA in the center of iron-containing lesions with a distinct rim compared to non-iron lesions, reflecting more severe tissue damage. Furthermore, in newly

emerging lesions with iron-accumulation, the tNAA decrease was persistent on a follow-up scan in contrast to non-iron lesions, where tNAA slightly recovered on a follow-up scan. Future studies should, therefore, take different types of iron accumulation into account, as each type is likely associated with a different level of tissue damage, as indicated by the very different metabolic profiles.

References

[1] C. H. Polman *et al.*, “Diagnostic criteria for multiple sclerosis: 2010 Revisions to the McDonald criteria,” *Ann. Neurol.*, vol. 69, no. 2, pp. 292–302, 2011, doi: https://doi.org/10.1002/ana.22366.

[2] A. J. Thompson *et al.*, “Diagnosis of multiple sclerosis: 2017 revisions of the McDonald criteria,” *Lancet Neurol.*, vol. 17, no. 2, pp. 162–173, Feb. 2018, doi: 10.1016/S1474-4422(17)30470-2.

[3] “Performance of the 2017 and 2010 Revised McDonald Criteria in Predicting MS Diagnosis After a Clinically Isolated Syndrome | Neurology.” https://n.neurology.org/content/98/1/e1.long (accessed Feb. 16, 2023).

[4] H. F. McFarland, “Correlation between MR and Clinical Findings of Disease Activity in Multiple Sclerosis,” *AJNR Am. J. Neuroradiol.*, vol. 20, no. 10, pp. 1777–1778, Nov. 1999.

[5] G. Öz *et al.*, “Clinical Proton MR Spectroscopy in Central Nervous System Disorders,” *Radiology*, vol. 270, no. 3, pp. 658–679, Mar. 2014, doi: 10.1148/radiol.13130531.

[6] G. Hangel, E. Niess, P. Lazen, P. Bednarik, W. Bogner, and B. Strasser, “Emerging methods and applications of ultra-high field MR spectroscopic imaging in the human brain,” *Anal. Biochem.*, vol. 638, p. 114479, Feb. 2022, doi: 10.1016/j.ab.2021.114479.

[7] N. De Stefano *et al.*, “Diffuse Axonal and Tissue Injury in Patients With Multiple Sclerosis With Low Cerebral Lesion Load and No Disability,” *Arch. Neurol.*, vol. 59, no. 10, p. 1565, Oct. 2002, doi: 10.1001/archneur.59.10.1565.

[8] M. Filippi *et al.*, “Evidence for widespread axonal damage at the earliest clinical stage of multiple sclerosis,” *Brain J. Neurol.*, vol. 126, no. Pt 2, pp. 433–437, Feb. 2003, doi: 10.1093/brain/awg038.

[9] I. I. Kirov, V. Patil, J. S. Babb, H. Rusinek, J. Herbert, and O. Gonen, “MR Spectroscopy Indicates Diffuse Multiple Sclerosis Activity During Remission,” *J. Neurol. Neurosurg. Psychiatry*, vol. 80, no. 12, p. 1330, Dec. 2009, doi: 10.1136/jnnp.2009.176263.

[10] M. S. Martire, L. Moiola, M. A. Rocca, M. Filippi, and M. Absinta, “What is the potential of paramagnetic rim lesions as diagnostic indicators in multiple sclerosis?,” *Expert Rev. Neurother.*, vol. 22, no. 10, pp. 829–837, Oct. 2022, doi: 10.1080/14737175.2022.2143265.

[11] S. Hametner, A. Dal Bianco, S. Trattnig, and H. Lassmann, “Iron related changes in MS lesions and their validity to characterize MS lesion types and dynamics with Ultra-high field magnetic resonance imaging,” *Brain Pathol.*, vol. 28, no. 5, pp. 743–749, 2018, doi: 10.1111/bpa.12643.

[12] M. Absinta *et al.*, “Association of Chronic Active Multiple Sclerosis Lesions With Disability In Vivo,” *JAMA Neurol.*, vol. 76, no. 12, pp. 1474–1483, Dec. 2019, doi: 10.1001/jamaneurol.2019.2399.

[13] M. T. Fischer *et al.*, “Disease-specific molecular events in cortical multiple sclerosis lesions,” *Brain*, vol. 136, no. 6, pp. 1799–1815, Jun. 2013, doi: 10.1093/brain/awt110.

[14] S. Luchetti, N. L. Fransen, C. G. van Eden, V. Ramaglia, M. Mason, and I. Huitinga, "Progressive multiple sclerosis patients show substantial lesion activity that correlates with clinical disease severity and sex: a retrospective autopsy cohort analysis," *Acta Neuropathol. (Berl.)*, vol. 135, no. 4, pp. 511–528, Apr. 2018, doi: 10.1007/s00401-018-1818-y.

[15] M. Absinta *et al.*, "Persistent 7-tesla phase rim predicts poor outcome in new multiple sclerosis patient lesions," *J. Clin. Invest.*, vol. 126, no. 7, pp. 2597–2609, Jul. 2016, doi: 10.1172/JCI86198.

[16] H. Kolb, O. Al-Louzi, E. S. Beck, P. Sati, M. Absinta, and D. S. Reich, "From pathology to MRI and back: Clinically relevant biomarkers of multiple sclerosis lesions," *NeuroImage Clin.*, vol. 36, p. 103194, Jan. 2022, doi: 10.1016/j.nicl.2022.103194.

[17] A. Dal-Bianco *et al.*, "Slow expansion of multiple sclerosis iron rim lesions: pathology and 7 T magnetic resonance imaging," *Acta Neuropathol. (Berl.)*, vol. 133, no. 1, pp. 25–42, 2017, doi: 10.1007/s00401-016-1636-z.

[18] U. W. Kaunzner *et al.*, "Quantitative susceptibility mapping identifies inflammation in a subset of chronic multiple sclerosis lesions," *Brain*, vol. 142, no. 1, pp. 133–145, Jan. 2019, doi: 10.1093/brain/awy296.

[19] M. Filippi *et al.*, "Assessment of lesions on magnetic resonance imaging in multiple sclerosis: practical guidelines," *Brain*, vol. 142, no. 7, pp. 1858–1875, Jul. 2019, doi: 10.1093/brain/awz144.

[20] P. Maggi *et al.*, "Central vein sign differentiates Multiple Sclerosis from central nervous system inflammatory vasculopathies," *Ann. Neurol.*, vol. 83, no. 2, pp. 283–294, Feb. 2018, doi: 10.1002/ana.25146.

[21] T. R. Lim *et al.*, "Paramagnetic rim lesions predict the development of clinical MS in radiologically isolated syndrome: preliminary results from a prospective cohort study; ECTRIMS 2022 – Oral Presentations (O093)," *Mult. Scler. J.*, vol. 28, no. 3_suppl, pp. 3–129, Oct. 2022, doi: 10.1177/13524585221123685.

[22] M. A. Clarke *et al.*, "Value of 3T Susceptibility-Weighted Imaging in the Diagnosis of Multiple Sclerosis," *Am. J. Neuroradiol.*, vol. 41, no. 6, pp. 1001–1008, Jun. 2020, doi: 10.3174/ajnr.A6547.

[23] A. Dal-Bianco *et al.*, "Slow expansion of multiple sclerosis iron rim lesions: pathology and 7 T magnetic resonance imaging," *Acta Neuropathol. (Berl.)*, vol. 133, no. 1, pp. 25–42, 2017, doi: 10.1007/s00401-016-1636-z.

[24] A. Dal-Bianco *et al.*, "Long-term evolution of multiple sclerosis iron rim lesions in 7 T MRI," *Brain*, vol. 144, no. 3, pp. 833–847, Mar. 2021, doi: 10.1093/brain/awaa436.

[25] M. Absinta and A. Dal-Bianco, "Slowly expanding lesions are a marker of progressive MS – Yes," *Mult. Scler. J.*, vol. 27, no. 11, pp. 1679–1681, Oct. 2021, doi: 10.1177/13524585211013748.

[26] D. L. Arnold, S. Belachew, A. R. Gafson, L. Gaetano, C. Bernasconi, and C. Elliott, "Slowly expanding lesions are a marker of progressive MS - No," *Mult. Scler. Houndmills*

Basingstoke Engl., vol. 27, no. 11, pp. 1681–1683, Oct. 2021, doi: 10.1177/13524585211017020.

[27] C. Enzinger, “Slowly expanding lesions are a marker of progressive MS – Commentary,” *Mult. Scler. J.*, vol. 27, no. 11, pp. 1683–1685, Oct. 2021, doi: 10.1177/13524585211040225.

[28] A. Lipka *et al.*, “Lesion-Specific Metabolic Alterations in Relapsing-Remitting Multiple Sclerosis Via 7 T Magnetic Resonance Spectroscopic Imaging,” *Invest. Radiol.*, p. 10.1097/RLI.0000000000000913, doi: 10.1097/RLI.0000000000000913.

[29] J. F. Kurtzke, “On the origin of EDSS,” *Mult. Scler. Relat. Disord.*, vol. 4, no. 2, pp. 95–103, Mar. 2015, doi: 10.1016/j.msard.2015.02.003.

[30] E. Heckova *et al.*, “7 T Magnetic Resonance Spectroscopic Imaging in Multiple Sclerosis: How Does Spatial Resolution Affect the Detectability of Metabolic Changes in Brain Lesions?,” *Invest. Radiol.*, vol. 54, no. 4, pp. 247–254, Apr. 2019, doi: 10.1097/RLI.0000000000000531.

[31] B. Strasser *et al.*, “(2 + 1)D-CAIPIRINHA accelerated MR spectroscopic imaging of the brain at 7T,” *Magn. Reson. Med.*, vol. 78, no. 2, pp. 429–440, 2017, doi: https://doi.org/10.1002/mrm.26386.

[32] G. Hangel *et al.*, “Ultra-high resolution brain metabolite mapping at 7 T by short-TR Hadamard-encoded FID-MRSI,” *NeuroImage*, vol. 168, pp. 199–210, Mar. 2018, doi: 10.1016/j.neuroimage.2016.10.043.

[33] S. M. Smith, “Fast robust automated brain extraction,” *Hum. Brain Mapp.*, vol. 17, no. 3, pp. 143–155, 2002, doi: https://doi.org/10.1002/hbm.10062.

[34] B. Strasser *et al.*, “Coil combination of multichannel MRSI data at 7 T: MUSICAL,” *NMR Biomed.*, vol. 26, no. 12, pp. 1796–1805, 2013, doi: https://doi.org/10.1002/nbm.3019.

[35] B. Bilgic *et al.*, “Fast Image Reconstruction with L2-Regularization,” *J. Magn. Reson. Imaging JMRI*, vol. 40, no. 1, pp. 181–191, Jul. 2014, doi: 10.1002/jmri.24365.

[36] A. Naressi *et al.*, “Java-based graphical user interface for the MRUI quantitation package,” *Magn. Reson. Mater. Phys. Biol. Med.*, vol. 12, no. 2, p. 141, Jun. 2001, doi: 10.1007/BF02668096.

[37] M. Považan *et al.*, “Mapping of brain macromolecules and their use for spectral processing of 1H-MRSI data with an ultra-short acquisition delay at 7T,” *NeuroImage*, vol. 121, pp. 126–135, Nov. 2015, doi: 10.1016/j.neuroimage.2015.07.042.

[38] A. Lin *et al.*, “Minimum Reporting Standards for in vivo Magnetic Resonance Spectroscopy (MRSinMRS): Experts’ consensus recommendations,” *NMR Biomed.*, vol. 34, no. 5, p. e4484, 2021, doi: 10.1002/nbm.4484.

[39] P. A. Yushkevich *et al.*, “User-guided 3D active contour segmentation of anatomical structures: Significantly improved efficiency and reliability,” *NeuroImage*, vol. 31, no. 3, pp. 1116–1128, Jul. 2006, doi: 10.1016/j.neuroimage.2006.01.015.

[40] C. Tozlu *et al.*, “Structural disconnectivity from paramagnetic rim lesions is related to disability in multiple sclerosis,” *Brain Behav.*, vol. 11, no. 10, p. e2353, Sep. 2021, doi: 10.1002/brb3.2353.

[41] E. Stephenson, N. Nathoo, Y. Mahjoub, J. F. Dunn, and V. W. Yong, “Iron in multiple sclerosis: roles in neurodegeneration and repair,” *Nat. Rev. Neurol.*, vol. 10, no. 8, Art. no. 8, Aug. 2014, doi: 10.1038/nrneurol.2014.118.

[42] A. Lipka *et al.*, “Ultra-high field MR spectroscopic imaging... - Google Scholar,” presented at the Int. Soc. Magn. Reson. Med. 29th Annu. Meet. (2021), p. 3349. Accessed: Feb. 16, 2023. [Online]. Available: https://lmy.de/SndZ2

[43] P. Maggi *et al.*, “Chronic White Matter Inflammation and Serum Neurofilament Levels in Multiple Sclerosis,” *Neurology*, vol. 97, no. 6, pp. e543–e553, Aug. 2021, doi: 10.1212/WNL.0000000000012326.

[44] I. I. Kirov *et al.*, “Proton MR spectroscopy of lesion evolution in multiple sclerosis: Steady‐state metabolism and its relationship to conventional imaging,” *Hum. Brain Mapp.*, vol. 38, no. 8, pp. 4047–4063, May 2017, doi: 10.1002/hbm.23647.

[45] D. M. Harrison *et al.*, “Lesion Heterogeneity on High-Field Susceptibility MRI Is Associated with Multiple Sclerosis Severity,” *AJNR Am. J. Neuroradiol.*, vol. 37, no. 8, pp. 1447–1453, Aug. 2016, doi: 10.3174/ajnr.A4726.

[46] M. Marcille *et al.*, “Disease correlates of rim lesions on quantitative susceptibility mapping in multiple sclerosis,” *Sci. Rep.*, vol. 12, no. 1, Art. no. 1, Mar. 2022, doi: 10.1038/s41598-022-08477-6.

[47] A. I. Altokhis *et al.*, “Longitudinal clinical study of patients with iron rim lesions in multiple sclerosis,” *Mult. Scler. J.*, vol. 28, no. 14, pp. 2202–2211, Dec. 2022, doi: 10.1177/13524585221114750.

[48] C. A. Treaba *et al.*, “Cortical and phase rim lesions on 7 T MRI as markers of multiple sclerosis disease progression,” *Brain Commun.*, vol. 3, no. 3, p. fcab134, Jun. 2021, doi: 10.1093/braincomms/fcab134.

[49] L. Hingerl *et al.*, “Clinical High-Resolution 3D-MR Spectroscopic Imaging of the Human Brain at 7 T,” *Invest. Radiol.*, vol. 55, no. 4, pp. 239–248, Apr. 2020, doi: 10.1097/RLI.0000000000000626.

[50] E. E. Brief, I. M. Vavasour, C. Laule, D. K. B. Li, and A. L. MacKay, “Proton MRS of large multiple sclerosis lesions reveals subtle changes in metabolite T1 and area,” *NMR Biomed.*, vol. 23, no. 9, pp. 1033–1037, 2010, doi: 10.1002/nbm.1527.

Tables and Figures

Characteristic	Participants with RRMS (n = 31)
Sex	
Male	15
Female	16
Age (y) *	36.9 ± 10.3 (21 - 55)
Disease Duration (months) *	109.42 ± 61.94 (2 - 229)
EDSS score †	1 (0 - 3.5)
No. of	
MS lesions °	487 (220)
non-iron °	412 (174)
area °	31 (13)
transition °	8 (7)
rim °	36 (26)
No. of participants receiving therapy	24
first-line	13
second-line	11

Table 1: Characteristics and Clinical Data of RRMS Patients
Note: Unless otherwise specified, data are numbers of participants.
* Data are means ± standard deviations; data in parentheses are ranges.
† Data are medians, with ranges in parentheses
° Data in parentheses define the number of lesions meeting the minimum size criterion

Characteristic	Participants with RRMS (n = 31)
No. of	
patients with newly emerging lesions	7
newly emerging lesions	39
non-iron	21
iron	18
lesions with spectroscopic data available	27
non-iron	11
iron	16

Table 2: Characteristics of data for the evaluation of newly emerging lesions

mIns/tNAA

vs.	NAWM (0.53±0.17)	non-iron (1.13±0.58)	area (0.93±0.30)	transition (1.04±0.42)	rim (1.53±0.97)
NAWM	-				
non-iron	**0.0000**	-			
area	0.287	0.783	-		
transition	0.249	0.994	0.995	-	
rim	**0.0000**	**0.021**	**0.035**	0.301	-

mIns/tCr

vs.	NAWM (0.85±0.30)	non-iron (1.08±0.36)	area (1.19±0.49)	transition (1.14±0.38)	rim (1.19±0.37)
NAWM	-				
non-iron	**0.012**	-			
area	**0.040**	0.823	-		
transition	0.311	0.991	0.999	-	
rim	**0.005**	0.615	1.00	0.311	-

tNAA/tCr

vs.	NAWM (1.67±0.37)	non-iron (1.08±0.39)	area (1.37±0.62)	transition (1.16±0.52)	rim (1.00±0.47)
NAWM	-				
non-iron	**0.0000**	-			
area	0.235	0.139	-		
transition	**0.035**	0.987	0.828	-	
rim	**0.0000**	0.891	*0.051*	0.887	-

tCho/tCr

vs.	NAWM (0.46±0.08)	non-iron (0.42±0.07)	area (0.43±0.08)	transition (0.45±0.05)	rim (0.40±0.10)
NAWM	-				
non-iron	*0.056*	-			
area	0.750	0.991	-		
transition	0.985	0.931	0.996	-	
rim	**0.009**	0.432	0.602	0.521	-

Table 3: p-values of the Iron Accumulation Type Comparison. Mirrored cells (dark gray) were left out for better readability of the table. All metabolic concentration ratio values are listed as mean+-SD.

mIns/tNAA

vs.	L+3_non-iron (1.00±0.00)	L0_non-iron (1.11±0.11)	L-3_non-iron (1.15±0.26)	L+3_iron (1.00±0.00)	L0_iron (1.23±0.11)	L-3_iron (1.40±0.34)
L+3_non-iron	-					
L0_non-iron	*0.077*	-				
L-3_non-iron	**0.0013**	0.995	-			
L+3_iron	1.000			-		
L0_iron		0.809		0.196	-	
L-3_iron			0.0046	**0.0001**	0.628	-

mIns/tCr

vs.	L+3_non-iron (1.00±0.00)	L0_non-iron (1.01±0.07)	L-3_non-iron (1.00±0.15)	L+3_iron (1.00±0.00)	L0_iron (1.05±0.07)	L-3_iron (1.03±0.10)
L+3_non-iron	-					
L0_non-iron	1.000	-				
L-3_non-iron	1.000	1.000	-			
L+3_iron	1.000			-		
L0_iron		0.995		0.998	-	
L-3_iron			1.000	1.000	1.000	-

tNAA/tCr

vs.	L+3_non-iron (1.00±0.00)	L0_non-iron (0.89±0.11)	L-3_non-iron (0.85±0.29)	L+3_iron (1.00±0.00)	L0_iron (0.83±0.08)	L-3_iron (0.65±0.16)
L+3_non-iron	-					
L0_non-iron	*0.065*	-				
L-3_non-iron	**0.0005**	0.986	-			
L+3_iron	1.000			-		
L0_iron		0.998		0.611	-	
L-3_iron			0.048	**0.0005**	0.507	-

tCho/tCr

vs.	L+3_non-iron (1.00±0.00)	L0_non-iron (0.99±0.07)	L-3_non-iron (0.98±0.11)	L+3_iron (1.00±0.00)	L0_iron (0.96±0.05)	L-3_iron (0.91±0.08)
L+3_non-iron	-					
L0_non-iron	1.000	-				

L-3_non-iron	0.999	1.000	-			
L+3_iron	1.000			-		
L0_iron		0.999		0.996	-	
L-3_iron			0.384	0.4530	0.991	-

Table 4: p-values of the Lesion Periphery Analysis. Mirrored cells (dark gray) were left out for better readability of the table. Light gray cells reflect comparisons between iron types within the respective layer, which are depicted only once for better readability. All metabolic concentration ratio values are listed as mean+-SD.

mIns/tNAA

vs.	Year-1_all_new (0.74±0.31)	Year0_all_new (1.17±0.41)	Year1_all_new (1.26±0.76)
Year-1_all_new	-		
Year0_all_new	0.126	-	
Year1_all_new	**0.049**	0.904	-

vs.	Year-1_iron (0.73±0.22)	Year0_iron (1.41±0.35)	Year1_iron (1.33±0.82)
Year-1_iron	-		
Year0_iron	*0.087*	-	
Year1_iron	0.108	0.957	-

vs.	Year-1_non-iron (0.75±0.44)	Year0_non-iron (0.85±0.24)	Year1_non-iron (1.05±0.59)
Year-1_non-iron	-		
Year0_non-iron	0.921	-	
Year1_non-iron	0.556	0.748	-

vs.	Year-1_non-iron (0.75±0.44)	Year0_non-iron (0.85±0.24)	Year1_non-iron (1.05±0.59)
Year-1_iron (0.73±0.22)	1.000		
Year0_iron (1.41±0.35)		0.403	
Year1_iron (1.33±0.82)			0.944

mIns/tCr

vs.	Year-1_all_new (0.84±0.35)	Year0_all_new (0.94±0.32)	Year1_all_new (1.03±0.19)
Year-1_all_new	-		
Year0_all_new	0.557	-	
Year1_all_new	0.160	0.667	-

vs.	Year-1_iron (0.82±0.32)	Year0_iron (1.11±0.35)	Year1_iron (1.06±0.16)
Year-1_iron	-		
Year0_iron	*0.084*	-	
Year1_iron	0.136	0.909	-

vs.	Year-1_non-iron (0.86±0.40)	Year0_non-iron (0.79±0.20)	Year1_non-iron (0.95±0.25)
Year-1_non-iron	-		
Year0_non-iron	0.866	-	

vs.	Year-1_non-iron (0.86±0.40)	Year0_non-iron (0.79±0.20)	Year1_non-iron (0.95±0.25)
Year-1_iron (0.82±0.32)	1.000		
Year0_iron (1.11±0.35)		0.190	

Year1_non-iron	0.884	0.632	-

Year1_iron (1.06±0.16)	0.984

tNAA/tCr

vs.	Year-1_all_new (1.30±0.34)	Year0_all_new (0.90±0.19)	Year1_all_new (0.97±0.31)
Year-1_all_new	-		
Year0_all_new	**0.0004**	-	
Year1_all_new	**0.006**	0.774	-

vs.	Year-1_iron (1.22±0.29)	Year0_iron (0.84±0.19)	Year1_iron (0.92±0.27)
Year-1_iron	-		
Year0_iron	**0.013**	-	
Year1_iron	**0.041**	0.790	-

vs.	Year-1_non-iron (1.42±0.38)	Year0_non-iron (0.94±0.20)	Year1_non-iron (1.08±0.41)
Year-1_non-iron	-		
Year0_non-iron	**0.022**	-	
Year1_non-iron	0.231	0.762	-

vs.	Year-1_non-iron (1.42±0.38)	Year0_non-iron (0.94±0.20)	Year1_non-iron (1.08±0.41)
Year-1_iron (1.22±0.29)	0.699		
Year0_iron (0.84±0.19)		0.972	
Year1_iron (0.92±0.27)			0.930

tCho/tCr

vs.	Year-1_all_new (0.52±0.09)	Year0_all_new (0.53±0.09)	Year1_all_new (0.47±0.05)
Year-1_all_new	-		
Year0_all_new	0.937	-	
Year1_all_new	0.197	0.096	-

vs.	Year-1_iron (0.50±0.05)	Year0_iron (0.52±0.09)	Year1_iron (0.46±0.05)
Year-1_iron	-		
Year0_iron	0.815	-	
Year1_iron	0.221	*0.077*	-

vs.	Year-1_non-iron (0.54±0.13)	Year0_non-iron (0.53±0.09)	Year1_non-iron (0.50±0.06)
Year-1_non-iron	-		
Year0_non-iron	0.992	-	
Year1_non-iron	0.792	0.825	-

vs.	Year-1_non-iron (0.54±0.13)	Year0_non-iron (0.53±0.09)	Year1_non-iron (0.50±0.06)
Year-1_iron (0.50±0.05)	0.948		
Year0_iron (0.52±0.09)		1.000	
Year1_iron (0.46±0.05)			0.954

Table 5: p-values of the Newly Emerging Lesions Analysis. Mirrored cells (dark gray) were left out for better readability of the table. Light gray cells reflect comparisons between iron types within the respective year. All metabolic concentration ratio values are listed as mean+-SD.

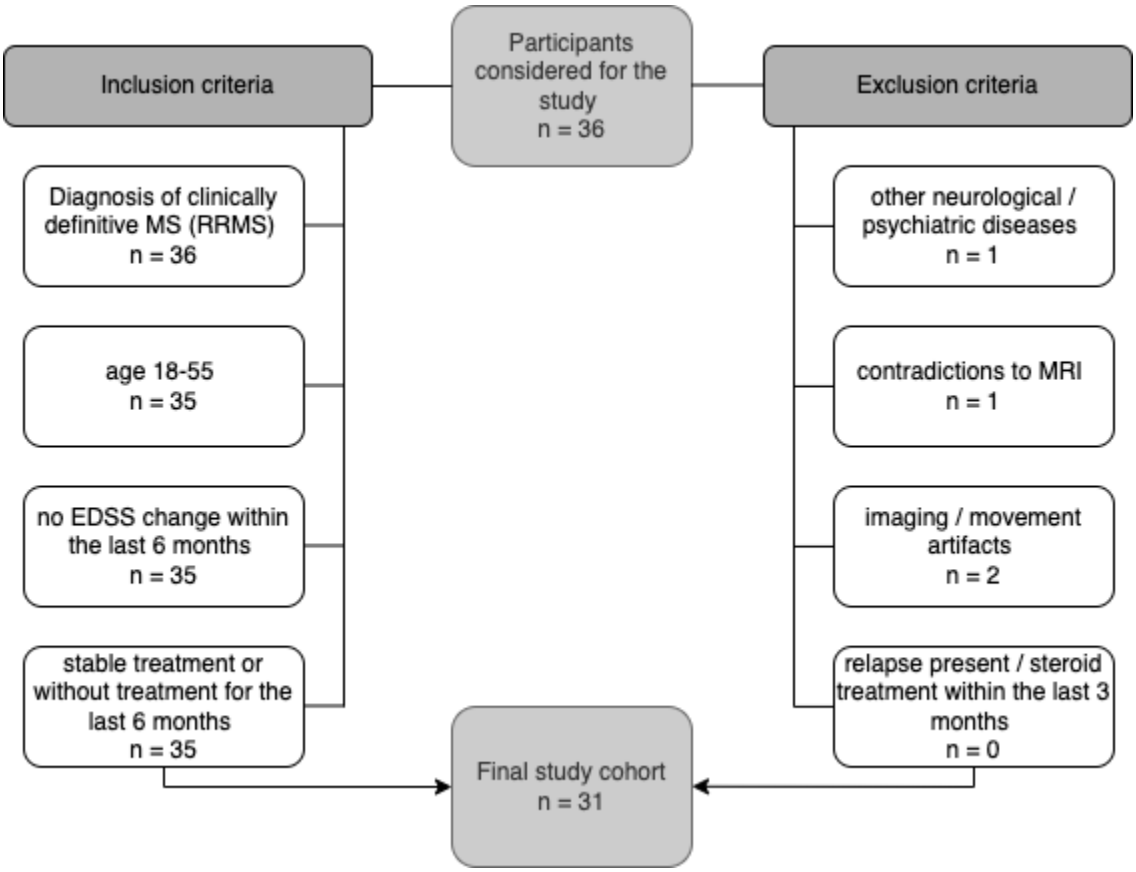

Figure 1: Flowchart of participants with MS enrolled in the study. EDSS = Expanded Disability Status Scale; MS = multiple sclerosis

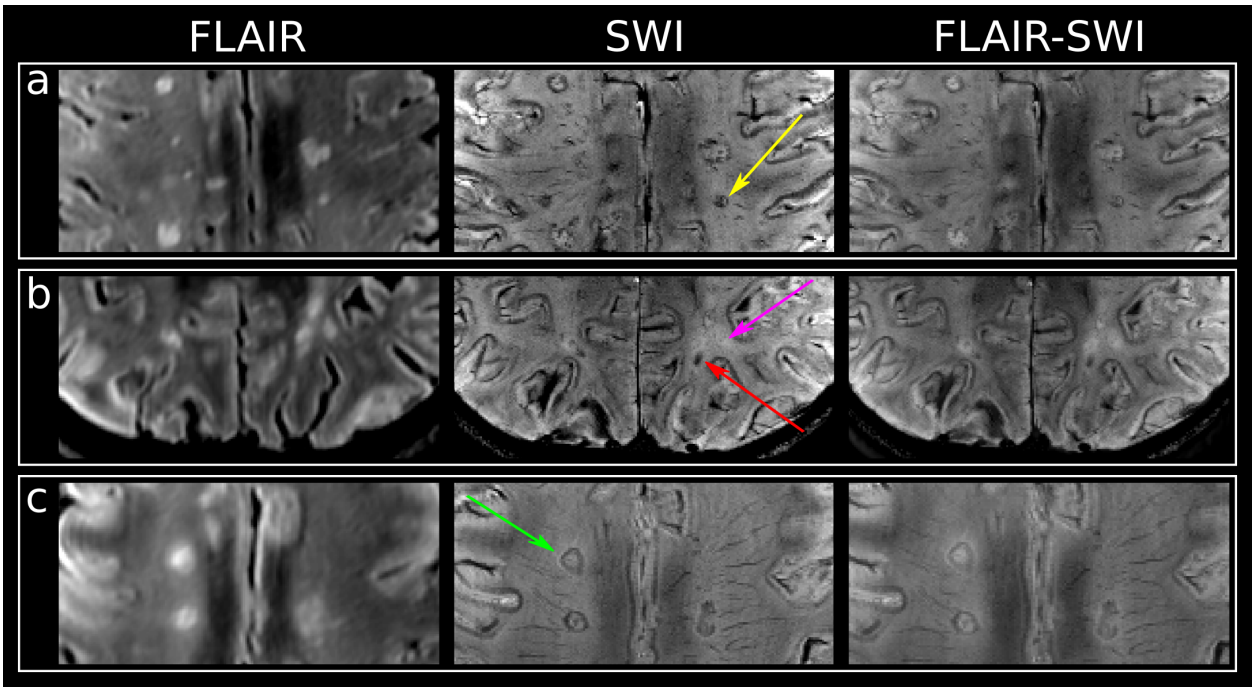

Figure 2: T2-FLAIR, SWI, and overlaid FLAIR-SWI images of (a) lesions categorized as “transition” with yellow arrow pointing toward an example, (b) “area” iron deposition indicated by a red arrow, “non-iron” indicated by a pink arrow, and (c) “rim” lesion with an iron rim indicated by a green arrow.

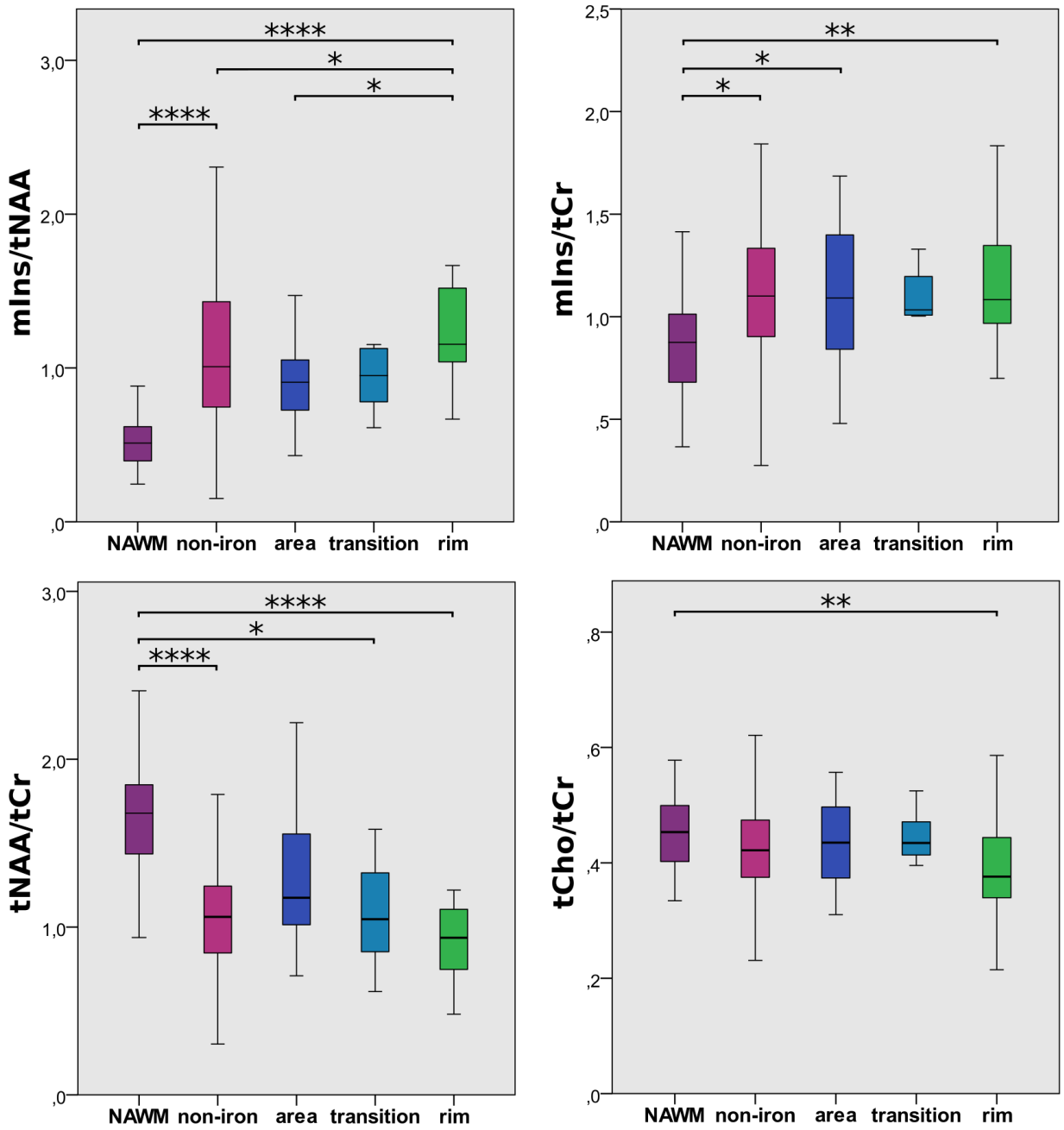

Figure 3: Boxplot diagram for mIns/tNAA, mIns/tCr, tNAA/tCr, and tCho/tCr of the NAWM and the different lesion categories “non-iron,”, “area,” “transition,” and “rim.” Significant differences were found, in particular, for mIns/tNAA and tNAA/tCr.

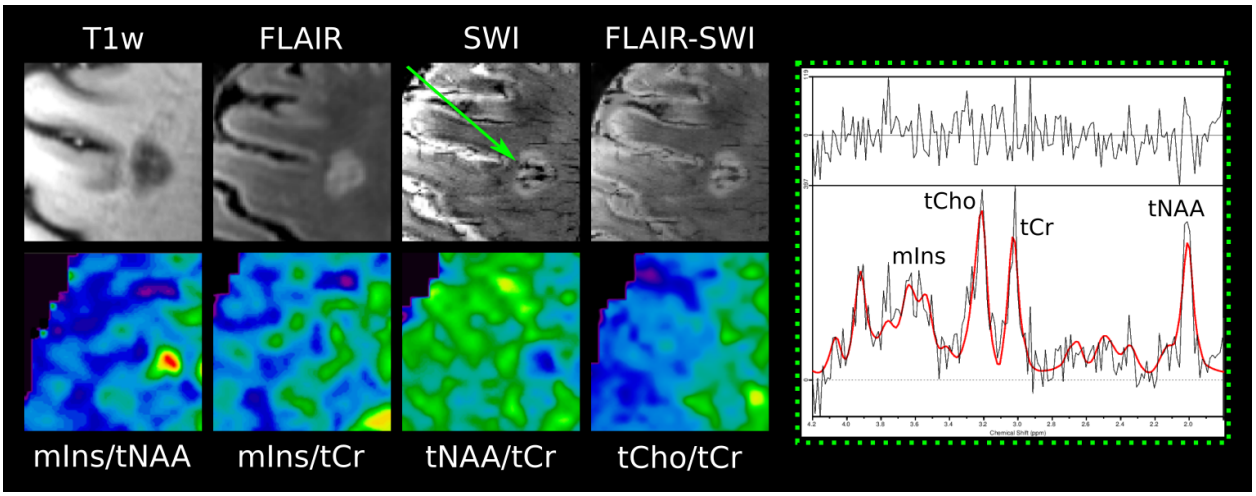

Figure 4: Examples of T1-weighted MP2RAGE, T2-weighted FLAIR, SWI, and overlaid FLAIR-SWI, as well as metabolic maps of mIns/tNAA, mIns/tCr, tNAA/tCr, and tCho/tCr and the MR spectrum of lesions. Green arrow points toward a “rim” lesion, which is clearly visible on mIns/tNAA and tNAA/tCr.

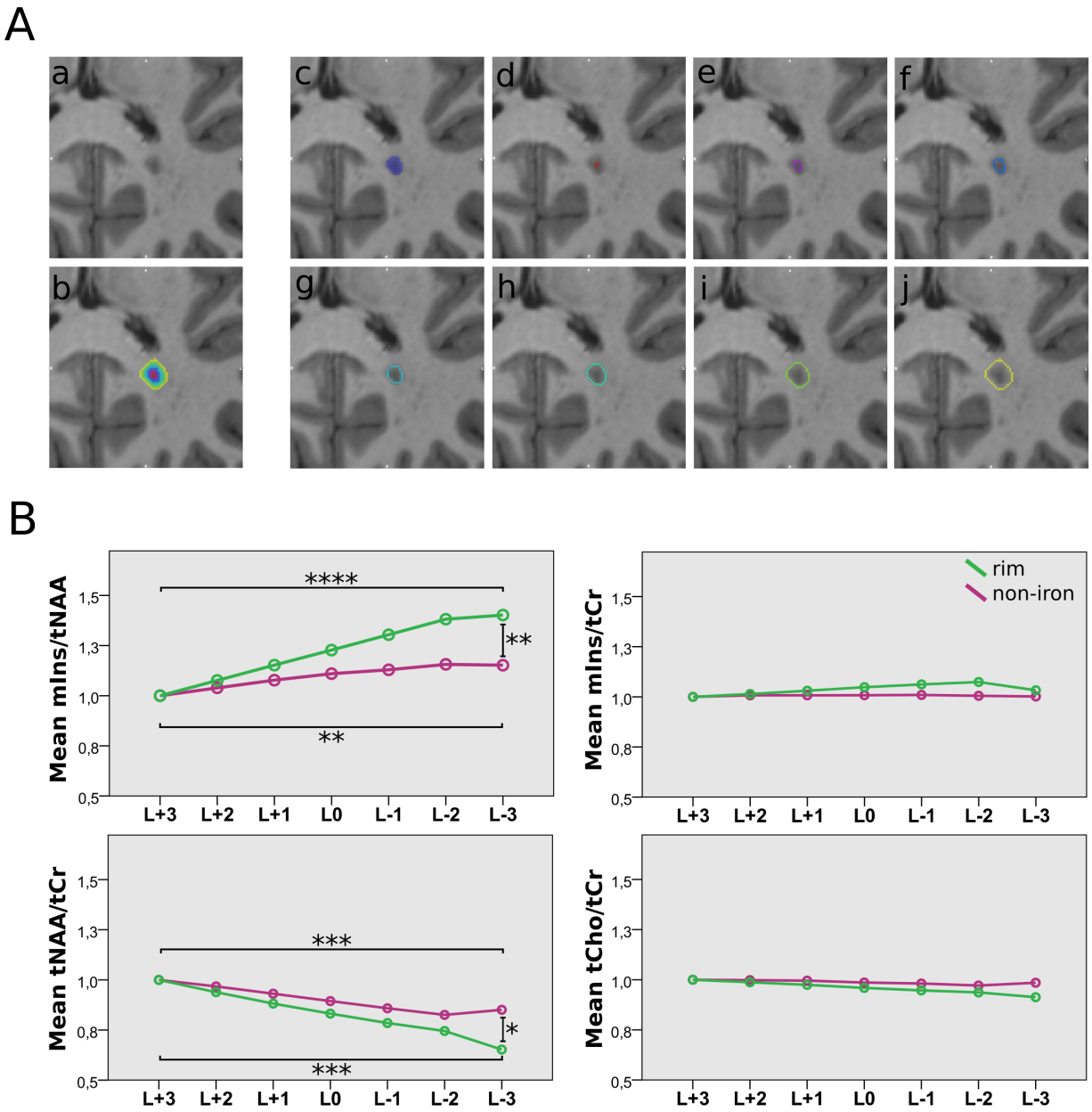

Figure 5:
A: An example of an MS lesion (a) and seven lesion layer rings (d)-(j) created by dilation/erosion of the segmented mask (c) using mincmorph. Dilation of lesions close to the GM or cerebrospinal fluid (CSF) can potentially lead to a lesion layer ring intruding into the GM or CSF; thus, lesion-free GM and CSF masks were created using Freesurfer and mincmath. To cancel out intruding voxels, these lesion-free masks were subtracted from the dilated lesion layer rings. Manual corrections with FSLView were performed if necessary. (b) All layer rings merged.
B: Boxplot diagram of normalized metabolic ratios show differences in mIns/tNAA and tNAA/tCr between the lesion layers of “rim” and “non-iron” lesions. Metabolic ratios of all layers were normalized to the outermost layer (L+3). Only significant results between L+3, L0, and L-3 are shown.

A

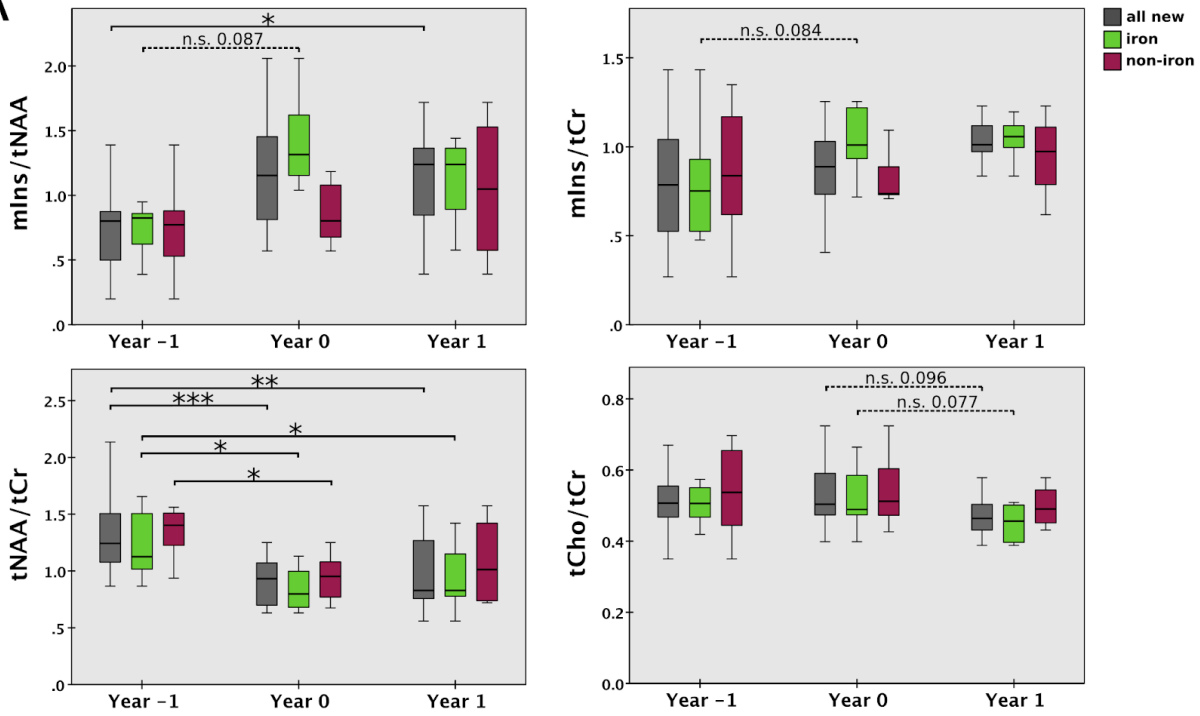

B

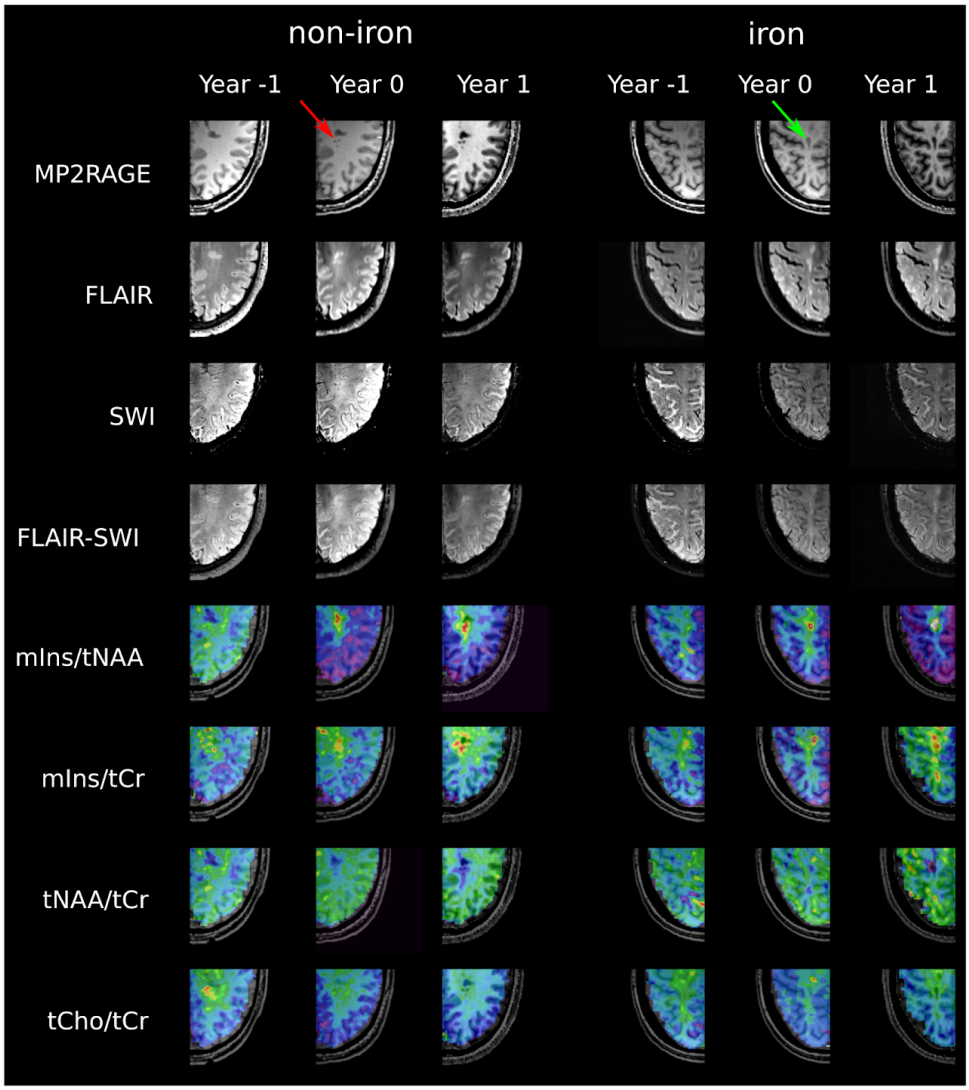

Figure 6:

A: Boxplot diagram for mIns/tNAA, mIns/tCr, tNAA/tCr, and tCho/tCr of newly emerging "non-iron" and "iron" lesions (also of joint "all new" group) for "Year -1" "Year 0," and "Year 1." Significant results were found especially for tNAA/tCr.

B: T1-weighted MP2RAGE, T2-weighted FLAIR, SWI, and overlaid FLAIR-SWI, as well as metabolic maps of mIns/tNAA, mIns/tCr, tNAA/tCr, and tCho/tCr for an exemplary "non-iron" and "iron" lesion at the yearly follow-up ("Year -1," "Year 0," and "Year 1").